Research Article

Nano Research
2020, 13(3): 810–817

ISSN 1998-0124 CN 11-5974/O4
https://doi.org/10.1007/s12274-020-2701-4

# Self-transforming ultrathin α-$Co(OH)_2$ nanosheet arrays from metal-organic framework modified graphene oxide with sandwich-like structure for efficient electrocatalytic oxygen evolution

Mengqiu Huang[1], Weiwei Liu[2,†], Lei Wang[1], Jiwei Liu[1], Guanyu Chen[1], Wenbin You[1], Jie Zhang[1], Lijun Yuan[2], Xuefeng Zhang[2], and Renchao Che[1] (✉)

[1] *Laboratory of Advanced Materials, Department of Materials Science and Collaborative Innovation Center of Chemistry for Energy Materials (iChem), Fudan University, Shanghai 200438, China*
[2] *College of Materials and Environmental Engineering, Hangzhou Dianzi University, Hangzhou 310012, China*
[†] *Present address: Laboratory of Advanced Materials, Department of Materials Science and Collaborative Innovation Center of Chemistry for Energy Materials (iChem), Fudan University, Shanghai 200438, China*


**Received:** 9 October 2019 / **Revised:** 2 February 2020 / **Accepted:** 6 February 2020

## ABSTRACT

Developing efficient and low-cost electrocatalysts for oxygen evolution reaction (OER) with high electrochemical activity and durability for diverse renewable and sustainable energy technologies remains challenging. Herein, an ultrasonic-assisted and coordination modulation strategy is developed to construct sandwich-like metal-organic framework (MOF) derived hydroxide nanosheet (NS) arrays/graphene oxide (GO) composite via one-step self-transformation route. Inducing from unsteady state, the dodecahedral ZIF-67 with $Co^{2+}$ in tetrahedral coordination auto-converts into defect-rich ultrathin layered hydroxides with the interlayered ion $NO_3^-$. The self-transforming α-$Co(OH)_2$/GO nanosheet arrays from ZIF-67 ($Co(OH)_2$-GNS) change the coordination mode of $Co^{2+}$ and bring about the exposure of more metal active sites, thereby enhancing the spatial utilization ratio within the framework. As monometal-based electrocatalyst, the optimized $Co(OH)_2$-GNS exhibits remarkable OER catalytic performance evidenced by a low overpotential of 259 mV to achieve a current density of 10 mA·cm$^{-2}$ in alkaline medium, even exceeding commercial $RuO_2$. During the oxygen evolution process, electron migration can be accelerated by the interfacial/in-plane charge polarization and local electric field, corroborated by the off-axis electron holography. Density functional theory (DFT) calculations further studied the collaboration between ultrathin $Co(OH)_2$ NS and GO, which leads to lower energy barriers of intermediate products and greatly promotes electrocatalytic property.

## KEYWORDS

metal-organic framework, oxygen evolution reaction, ultrathin nanosheet arrays, cobaltous hydroxide, charge transfer

## 1 Introduction

Oxygen evolution reaction (OER) is an essential reaction that is applied in many renewable electrochemical energy conversion systems and storage systems, such as water splitting, fuel cells, metal-air batteries and so on, which can alleviate the cosmopolitan energy and related environmental issue [1, 2]. However, in fact, the electrochemical progress has been hindered by its sluggish kinetics with a multiple electron-proton process and large overpotential, which have a bearing on breaking O–H bond breaking and forming O–O bond [3–5]. To date, Ir- and Ru-based materials are often applied in OER electrocatalysts and exhibit unrivalled catalytic performance [6], but suffer from their scarcity, prohibitive cost and low durability, which obstructs the wide practical applications. Hence, it is eager to construct cost-effective, highly efficient and enduring nonnoble-metal OER electrocatalysts for widespread use of renewable energy technologies.

Metal-organic framework (MOF) is a combination of joining metal atom nodes and organic ligands and used in gas storage and separation, biosensors, and catalysis field. Due to the high specific surface area, adjustable pore size and controllable structures, MOFs have considered as a new type of promising crystalline materials [7–11]. Currently, hydroxide-mimicking MOF, two-dimensional (2D) MOFs and hybrid MOF have attracted much attentions from researchers in the field of electrochemistry. For example, Tang et al. [12] reported ultrathin NiCo bimetallic MOF nanosheets (NSs) with coordinatively unsaturated metal atoms as promising electrocatalysts for OER process, which require a small overpotential of 250 mV at 10 mA·cm$^{-2}$ Ni-Co coupling effect. Zhao et al. [13] fabricated a generic approach to prepare the targeted 2D nickel-iron-MOF derived nanosheet arrays on diverse substrates to achieve intriguing electrocatalytic performance. Notwithstanding these merits, the applications of MOFs in electrocatalysis are hindered by low electrical conductivity, small pore size and encapsulated active metal centers by organic ligands [14]. Plenty of strategies have been proposed to improve the conductivity of MOF, such as pyrolysis at high temperatures, which loses the intrinsic active site of MOFs [9, 15].

Address correspondence to rcche@fudan.edu.cn

Ultrathin transition metal hydroxides (TMHs) are an important family of 2D nanomaterials, and attracted extensive attention as OER catalysts [16]. TMHs is a layered nanomaterial consisting of cationic brucite-like layers with replaceable charge-balancing anions between layers [17, 18]. The unique structure capacitates facile charge transport and highly exposed surface catalytic active sites, achieving high-performance electrocatalytic activity [19]. These advantages provide ultrathin 2D TMHs outstanding catalytic activities, even exceeding the costly and scarce reference noble metal oxide catalysts. However, up to now, few research focuses on converting MOFs into TMHs used for in OER electrocatalyst through self-transformation synthesize. Consequently, ultrathin MOF-derived 2D TMHs NSs are an ideal material to design efficient electrocatalysts. Based on retaining the intrinsic catalytic activity, size effect and increased exposed surface could produce much higher percentages of metal active sites in ultrathin MOF-derived 2D TMHs than that in original MOFs. Therefore, to design intriguing electrocatalysts with high conductivity, exploring new and highly efficient procedures is actually desirable, yet remains a serious issue. In addition, many attempts have been devoted to certifying the OER mechanism by the trapping position of charges in different indirect ways. Nevertheless, the technology to observe the charge distribution and local electric field is limited. In view of our previous work [20, 21], electron holography is an effective tool to reveal the electrostatic potential distribution because the charges in the composite can change the phase of the penetrated electron wave and such phase disturbance can be obtained from the electron [22, 23].

Benefitting from the extraordinary mechanical strength and large specific surface area, graphene oxide (GO) has been well documented to an ideal support or hybrids for catalysts [24, 25]. Especially, a large amount of oxygen-containing functional groups on the surface of GO is propitious to disperse and absorb precursors. For instance, Liu et al. employed GO as a conductive substrate to *in situ* grow $MoS_x$, which exhibited enhanced electrocatalytic activity owing to the good dispersion and conductivity of GO matrix [26]. Herein, for the first time, a series of self-transforming ultrathin Co-based hydroxide nanosheets from ZIF-67 were decorated onside GO ($Co(OH)_2$-GNS) by one-step method, which promotes the OER performance. Highly conductivity GO serves as a carbon substrate to constrain the growth orientation of arrays evolution and to offer fast electron transportation in OER. Meanwhile, both theoretical and experimental results prove that the content of targeted on-site formative α-$Co(OH)_2$ arrays plays a vital role in the reduction reaction. Optimized ultrathin $Co(OH)_2$-GNS exhibits a high electroactivity and long-time stability among the OER process, possessing a low overpotential of 259 mV and activity retention even after 1,000 cycles. In $Co(OH)_2$-GNS system, the local electronic field and interfacial/in-plane polarization were successfully formed by the inhomogeneous distribution of charge density proved by the off-axis electron holography, which acts an essential role in mechanism analysis. This strategy offers a promising route to new-type MOF-derived electrocatalysts and new insights into the improvement of oxygen evolution reaction kinetics, which can ultimately enhance the performance of next-generation industrial electrocatalysts.

## 2 Results and discussion

### 2.1 Fabrication of sandwich-like ultrathin $Co(OH)_2$-GNS-*x*

The one-step preparation process of self-transforming α-$Co(OH)_2$ NS from ZIF-67 decorated on GO is illustrated in Fig. 1. Cobalt ions were firstly mixed with GO solution in methanol to be fully absorbed on the surface of the GO sheets. The key roles are the electrostatic interactions and chemical bond between cobalt ions and the functional group on the surface of GO [27]. Then a certain amount of 2-methylimidazole in methanol was dispersed into the above mixture and sonicated for 12 h. After that, the resultant material was washed and lyophilized, which was denoted as $Co(OH)_2$-GNS-*x*. *x* represents samples with different amount of $Co(NO_3)_2{\cdot}6H_2O$, 2-methylimidazole and methanol. The self-transformation from ZIF-67 to α-$Co(OH)_2$ NS can be obviously observed (Fig. 1), which was further studied by Co-ZIF-1 and Co-ZIF-2 prepared by changing the molar ratio of metal salt and organic linker. The NS structure appeared after the proportion of $Co^{2+}$ and 2-methylimidazole added up to 3:4 (Figs. S1(b) and S1(e) in the Electronic Supplementary Material (ESM)). The morphology evolution from dodecahedron to the self-assembled sphere by NS is in agreement with powder X-ray diffraction (XRD) patterns (Fig. S2 in the ESM). The evolution of coordination mode was further investigated by UV/Vis diffuse reflection spectroscopy (Fig. S3 in the ESM). The tetrahedral $Co^{2+}$ coordination features located at 603 and 545 nm become gradually weaker, confirming the on-site transform dodecahedral ZIF-67 into α-$Co(OH)_2$ NS along with the coordination mode changing and phase transformation [14].

Phase transformation of the as-prepared composite materials was further investigated by XRD. Unlike ZIF-67, no sharp peaks are observed in $Co(OH)_2$-GNS-*x* and α-$Co(OH)_2$ NS samples (Fig. 2(a) and Fig. S4 in the ESM), corresponding to the layered α-$Co(OH)_2$ component (PDF, card no. 46-0605) with low crystallinity. A set of broad diffraction peaks at 10.62°, 21.88°, 34.16° and 59.7° can be consistent with the (003), (006), (102), and (110) reflections of the α-$Co(OH)_2$ phase, respectively [28]. Obviously, only one evident (002) peak is observed at around 10.35° in GO (Fig. 2(a)), which is covered in $Co(OH)_2$-GNS-*x* samples [29]. Additionally, the pore structure information on the $Co(OH)_2$-GNS-3 specimen was analyzed by $N_2$ sorption. A distinct hysteresis loop in the isotherm of the $Co(OH)_2$-GNS-3 catalyst suggests the existence of a mass of mesopores (Fig. S5 in the ESM). The Brunauer–Emmett–Teller (BET) specific surface area of $Co(OH)_2$-GNS-3 is measured to be 220 $m^2{\cdot}g^{-1}$ while the aperture is mainly concentrated at 3.8 nm

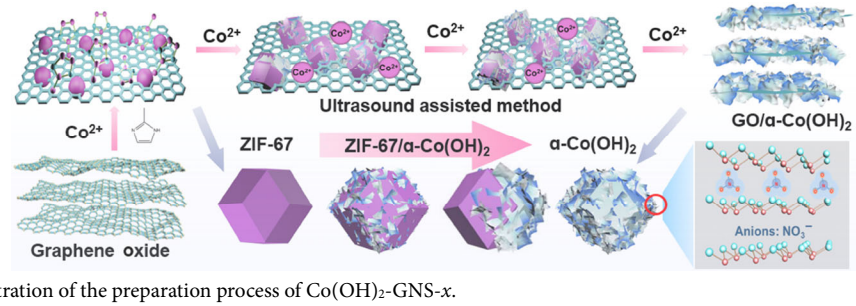


**Figure 1** Schematic illustration of the preparation process of $Co(OH)_2$-GNS-*x*.

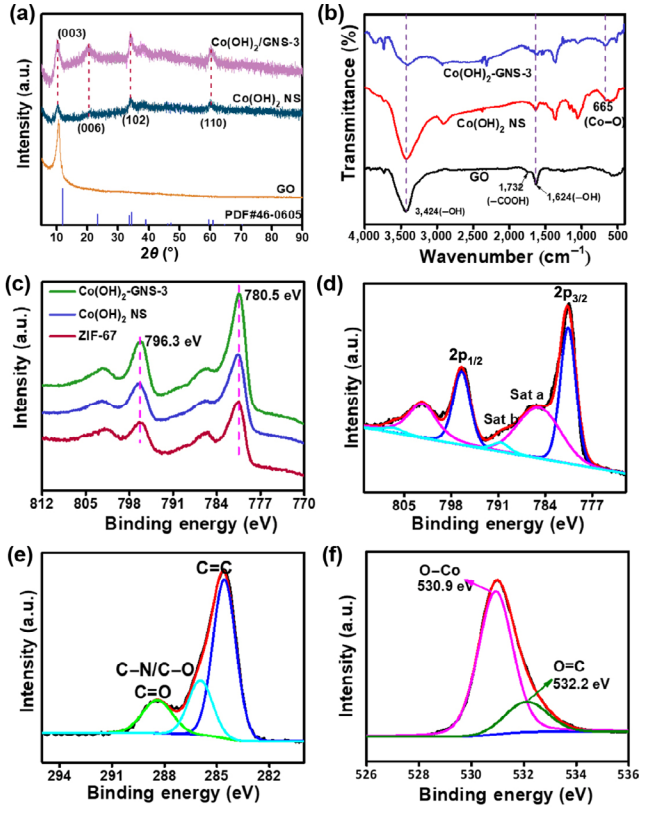


**Figure 2** XRD patterns (a) and FT-IR spectra (b) of GO, $Co(OH)_2$ NS and $Co(OH)_2$-GNS-3. XPS spectra of Co 2p (c) for ZIF-67, $Co(OH)_2$ NS and $Co(OH)_2$-GNS-3. High resolution XPS spectra of Co 2p (d), C 1s (e), O 1s (f) for $Co(OH)_2$-GNS-3.

(the inset of Fig. S5 in the ESM), resulting in electrocatalytic active sites exposure and efficient mass transport. To further gain insight into the structure of $Co(OH)_2$-GNS-*x*, Fourier-transformed infrared resonance (FT-IR) spectroscopy was measured to get more surface structural information. The peaks at 3,428, 1,736, and 1,642 $cm^{-1}$ of GO sample coincide with the stretching vibrations of hydroxyl, carboxyl, and O–H stretching vibration of interlayer water molecules, respectively (Fig. 2(b)) [30]. More importantly, the peak at 665 $cm^{-1}$, originates from the Co–O stretch in the α-$Co(OH)_2$ and $Co(OH)_2$-GNS samples [31].

The structure and morphology of $Co(OH)_2$-GNS samples were characterized by scanning electron microscopy (SEM), transmission electron microscopy (TEM) and atomic force microscopy (AFM). Figure 3 shows the morphology and element distribution of $Co(OH)_2$-GNS-3 samples. After adding the organic linker, a compact 2D NS is developed on the surface of the GO sheets forming a sandwich-like structure as a whole with a significant interface between GO and α-$Co(OH)_2$ NS (Figs. 3(a) and 3(b)). In line with the SEM images, a lateral structure is also revealed in the TEM image of $Co(OH)_2$-GNS-3 composites. The 2D interlaced nanoflakes are dense and uniformly stacked but not vertically grown on the surface of GO sheets, which is contributed to larger specific surface area (Figs. 3(c) and 3(d)). The high-resolution TEM (HRTEM) image displays a clear crystalline structure of 2D $Co(OH)_2$ NS proved by the clear lattice fringes and concentric circular rings of selected area electron diffraction (SAED) pattern (Fig. 3(e)). High-angle annular dark-field scanning transmission electron microscopy (HADDF-STEM) (Fig. 3(f)) mapping exhibits that Co, C, O and N elements are homogeneously distributed throughout the entire graphitic plate. The element of N comes from the interlayer anion $NO_3^-$ of α-$Co(OH)_2$. The loading content of α-$Co(OH)_2$ NS on the surface of GO can be facilely tuned, revealed from other samples (Figs. S6–S9 in the ESM). To accurately study the thickness of $Co(OH)_2$ NS, the $Co(OH)_2$-GNS-3 aqueous solution was put into a cell crusher for 30 min (Fig. S10 in the ESM). The thickness of nanolayers is determined to be ~ 3.4 nm by AFM (Fig. 3(g)) and HAADF-STEM image (Fig. 3(f)), suggesting the successful synthesis of the self-transforming ultrathin α-$Co(OH)_2$ NS from ZIF-67. Raman spectra were employed to interpret the composite graphitization degree. The peaks at 1,590 $cm^{-1}$ (G band) and 1,360 $cm^{-1}$ (D band) are allocated to the $sp^2$-bonded carbon atoms vibration and the defect-induced vibration, respectively [32, 33]. Compared to $Co(OH)_2$-GNS, the peaks of $Co(OH)_2$ at G band and D band are non-existent, indicating the GO was introduced successfully in $Co(OH)_2$-GNS. Besides, the intensity ratios between the D band and G band ($I_D/I_G$) of $Co(OH)_2$-GNS-*x* hybrids have no noticeable changes (1.09–1.12), which suggest GO was introduced successfully and the similar graphitized carbon structure in $Co(OH)_2$-GNS-*x* (Fig. S11 in the ESM).

Electron energy-loss spectroscopy (EELS) and X-ray photoelectron spectroscopy (XPS) were carried out to interpret elemental composition and valence state of the nanocomposite. The binding energies in Fig. 2(c) exist in almost the same position, suggesting the same chemical status of cobalt element in α-$Co(OH)_2$ NS, ZIF-67 and $Co(OH)_2$-GNS-3 samples. In the EELS curve of cobalt (Fig. S12 in the ESM), peaks $L_3$ and $L_2$ originate from the transition of electrons from $2p_{3/2}$ to $3d_{3/2}$ $3d_{5/2}$ and $2p_{1/2}$ to $3d_{3/2}$, and the integration ratio of $L_3/L_2$ was calculated by the Pearson method (the curve a in Fig. S12

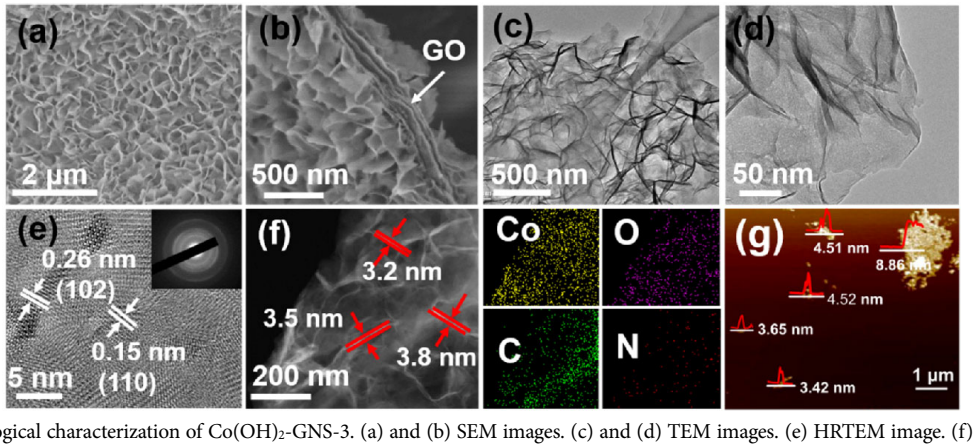


**Figure 3** Morphological characterization of $Co(OH)_2$-GNS-3. (a) and (b) SEM images. (c) and (d) TEM images. (e) HRTEM image. (f) The corresponding HAADF-STEM image and EDS mapping images of Co, C, N and O elements. (g) AFM images and corresponding height profile along the marked red lines of the ultrathin NS.

shows) and can be used to measure the oxidation level of Co; the valence decreases as the ratio increases.

These EELS spectra clearly show $L_3$ and $L_2$ edges of cobalt at 779.2 and 794.3 eV and the intensity ratio of the $L_3$ to $L_2$ peaks keeps around at 4.3, implying that the structure of $Co(OH)_2$-GNS-$x$ samples remains unchanged and chemical valence of cobalt in all compound is about +2 [34, 35], which is supported by XRD and XPS analysis. High-resolution XPS spectrum of Co 2p of $Co(OH)_2$-GNS-3 (Fig. 2(d)) shows that the binding energies at 780.4 and 796.3 eV coincide with Co $2p_{3/2}$ and Co $2p_{1/2}$, respectively [36]. According to the previous reports, the oxidation states of Co cations can also be judged by the energy gap between satellite peaks and main peaks. The energy gap of ~ 6.0 eV represents $Co^{2+}$ and 9–10 eV stands for $Co^{3+}$, suggesting the oxidation state of the cations in $Co(OH)_2$-GNS-$x$ is $Co^{2+}$. The high-resolution spectrum of C 1s for $Co(OH)_2$-GNS-3 (Fig. 2(e)) can be divided into three peaks at 284.6 (C=C), 285.9 (C–N) and 288.2 eV (C=O) [37], respectively, which come from graphene and remained dimethyl imidazole. O 1s spectrum of $Co(OH)_2$-GNS-3 composes of two distinctive peaks locating at 530.9 and 532.2 eV, arising from Co–O and C=O bonds (Fig. 2(f)) [38]. The high-resolution N 1s spectrum of Co-ZIF-2 reveals the appearance of five kinds of nitrogen species, including pyridinic N (398.5 eV), pyrrolic N (399.7 eV), quaternary-N (400.9 eV), graphitic N (402.8 eV) and $NO_3^-$ (406.7 eV) (Fig. S13 in the ESM) [39, 40]. After increasing the mole ratio of cobalt salt to form α-$Co(OH)_2$ NS, the peak intensities of pyridinic N, pyrrodic N, quaternary-N and graphitic N become extremely weak, suggesting the change of coordination mode between Co and dimethyl imidazole along with the phase transformation.

## 2.2 Electrochemical performance of ultrathin $Co(OH)_2$-GNS-3

The electrocatalytic activity of as-prepared materials toward OER was investigated in 1 M KOH at room temperature. Linear sweep voltammetry (LSV) was carried out to gain polarization curves of $Co(OH)_2$-GNS-$x$ and commercial catalysts ($RuO_2$) electrodes at a scan rate of 10 mV·s$^{-1}$ (Fig. 4(a)). Evidently, a detectable increased anodic current response started at an onset potential ($E_{onset}$, the potential to achieve 0.1 mA·cm$^{-2}$) of 1.42 V (vs. reversible hydrogen electrode, RHE) in $Co(OH)_2$-GNS-3 electrode, implying a remarkedly enhanced electrochemical activity compared to other samples. The $E_{onset}$ for $Co(OH)_2$-GNS-1, $Co(OH)_2$-GNS-2, $Co(OH)_2$-GNS-4, $Co(OH)_2$-GNS-5 and $RuO_2$ is 1.5, 1.49, 1.47, 1.5 and 1.45 V, respectively. Except for the $E_{onset}$ value, the potential at 10 mA·cm$^{-2}$ is usually used as a significant measurement for OER property. Using the thermodynamic OER potential ($E^0(H_2O/O_2)$ = 1.229 V) as a reference, the $Co(OH)_2$-GNS-3 shows a very low overpotential of only 259 mV at 10 mA·cm$^{-2}$, considerably smaller than that of $Co(OH)_2$-GNS-1 (369 mV), $Co(OH)_2$-GNS-2 (345 mV), $Co(OH)_2$-GNS-4 (324 mV), $Co(OH)_2$-GNS-5 (357 mV) and commercial $RuO_2$ (296 mV) (Fig. 4(a)), which exceed the pure GO, $Co(OH)_2$ specimens (Fig. S14 in the ESM), direct synthesized $Co(OH)_2$/GO (Fig. S15 in the ESM) and most of the reported monometal-based catalyst [41, 42]. Importantly, $Co(OH)_2$-GNS-3 possesses lower Tafel slope (85.9 mV·dec$^{-1}$) than other $Co(OH)_2$-GNS-$x$ catalysts including $Co(OH)_2$-GNS-1 (134 mV·dec$^{-1}$), $Co(OH)_2$-GNS-2 (101 mV·dec$^{-1}$), $Co(OH)_2$-GNS-4 (125 mV·dec$^{-1}$) and $Co(OH)_2$-GNS-5 (114 mV·dec$^{-1}$), indicating the marvelous intrinsic reaction kinetics of the $Co(OH)_2$-GNS-3 (Fig. 4(b)). In addition, electrochemical impedance spectroscopy (EIS) analysis was employed to interpret OER capability of the $Co(OH)_2$-GNS-$x$ from a dynamic point of view. The Nyquist plots suggest that the $Co(OH)_2$-GNS-3 shows a lowest impedance value (2.1 Ω) and holds a rapid proton-coupled electron transfer behavior than other catalysts (Fig. 4(c) and Fig. S16 in the ESM) [43].

The double-layer capacitance ($C_{dl}$) was studied by cyclic voltammograms (CVs) at different scan rate from 1.23 to 1.33 V without oxidation process at 20–100 mV·s$^{-1}$, which $C_{dl}$ is calculated at 1.28 V and can further obtain electrochemically active surface area (ECSA) values (Figs. S17 and S18 in the ESM). As can be seen from Fig. 4(d), $Co(OH)_2$-GNS-3 shows higher $C_{dl}$ (59 mF·cm$^{-2}$), compared to $Co(OH)_2$-GNS-1 (12.7 mF·cm$^{-2}$) and $Co(OH)_2$-GNS-2 (37.1 mF·cm$^{-2}$), corresponding to the higher ESCA value (1,475, Fig. S18 in the ESM). After increasing the loading content of MOF-derived $Co(OH)_2$ NS, the values of $C_{dl}$ of $Co(OH)_2$-GNS-4 (42 mF·cm$^{-2}$) and $Co(OH)_2$-GNS-5 (42 mF·cm$^{-2}$) are significantly decreased, indicating overloading of $Co(OH)_2$ NS in $Co(OH)_2$-GNS-4 and $Co(OH)_2$-GNS-5 (Figs. S8 and S9 in the ESM) and more exposure of catalytical active metal atoms in $Co(OH)_2$-GNS-3 hybrid. The normalized LSV curves on the sandwich-like catalysts by calculated ECSA reveal the enhancive performance, attributing to the raised ECSA (Fig. S19(a) in the ESM) [3]. The turnover frequency (TOF) value of $Co(OH)_2$-GNS-3 (0.242 s$^{-1}$) is much higher than that of $Co(OH)_2$-GNS-1 (0.086 s$^{-1}$), $Co(OH)_2$-GNS-2 (0.092 s$^{-1}$), $Co(OH)_2$-GNS-4 (0.088 s$^{-1}$) and $Co(OH)_2$-GNS-5 (0.041 s$^{-1}$), further confirming the excellent intrinsic activity of $Co(OH)_2$-GNS-3 (Fig. S19(b) in the ESM). The $Co(OH)_2$-GNS-3 exhibits the highest TOF value, resulting

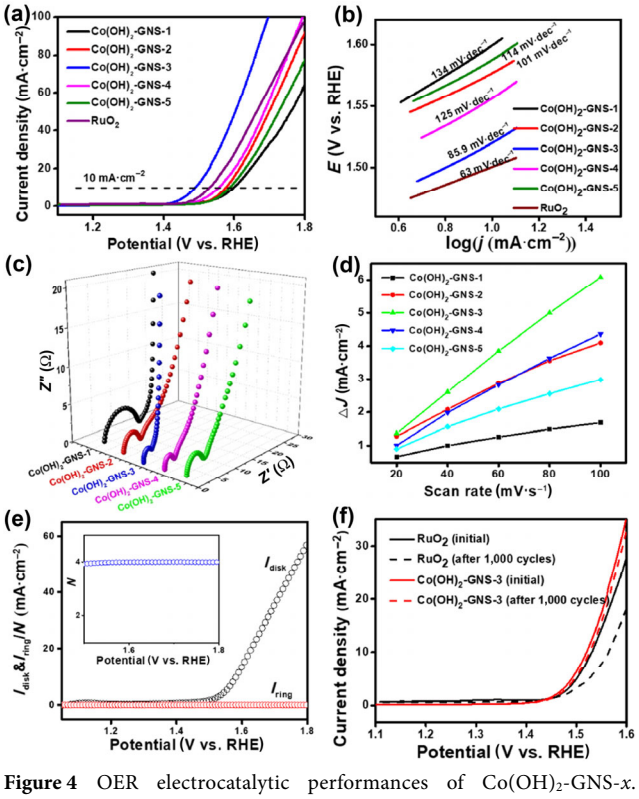


**Figure 4** OER electrocatalytic performances of $Co(OH)_2$-GNS-$x$. (a) Polarization curves and (b) corresponding Tafel plots of $Co(OH)_2$-GNS-$x$ ($x$ = 1, 2, 3, 4 and 5) and commercial $RuO_2$ in 1 M KOH with a scan rate of 10 mV·s$^{-1}$. (c) EIS Nyquist plots and current density difference (d) at 1.28 V plotted against scan rates of $Co(OH)_2$-GNS-$x$ ($x$ = 1, 2, 3, 4 and 5). (e) Rotating ring-disk electrode voltammogram obtained for $Co(OH)_2$-GNS-3 in 1 M KOH. The ring potential is set at 1.5 V vs. RHE to monitor the production of hydrogen peroxide; the inset of (e) shows the corresponding electron transfer number ($N$) as a function of applied potentials. (f) Polarization curves of $Co(OH)_2$-GNS-3 and $RuO_2$ at 10 mV·s$^{-1}$ before and after 1,000 cycles.

from combining conductive GO and the ultrathin NS with high surface area, mesoporous channels and maximizing the metal active sites. Compared with a disk current, no detectable current emerged on the ring electrode (Fig. 4(e)). The average electron transfer number (*N*) of $Co(OH)_2$-GNS-3 acquired through a rotating ring-disk electrode is 3.96, coinciding with an ideal four-electron pathway to generate oxygen [44]. As shown in Fig. S20 in the ESM, the $Co(OH)_2$-GNS-3 sample exhibits steady oxygen evolution rates that coincide well with theoretical volumes, indicating a nearly 100% Faradic efficiency of the Co-based electrocatalyst.

To further evaluate the stability of the catalysts, consecutive LSV scans are carried out in 1 M KOH. After 1,000 cycles, compared with $RuO_2$, the LSV curves proclaim that the $Co(OH)_2$-GNS-3 electrocatalyst can preserve good OER activity with very small shifts (Fig. 4(f)). The *j*–*t* measurement at 10 $mA{\cdot}cm^{-2}$ demonstrates high stability of the electrocatalyst as well (Fig. S21 in the ESM). TEM images (Figs. 5(a)–5(c)) and HADDF-STEM mapping (Fig. 5(d)) demonstrate the nearly unchanged structure and surface composition of $Co(OH)_2$-GNS-3 compound after 1,000 cycles electrocatalytic test, except that K element in STEM mapping comes from KOH electrolyte solution. However, the lower $L_3/L_2$ ratio (3.9) of $Co(OH)_2$-GNS-3 after OER than $Co(OH)_2$-GNS-3 (4.3) in EELS spectrum (Fig. 5(e)) represents a higher chemical valence of Co, which is consistent with the possibility of CoOOH formation [45]. The HRTEM images show no obvious lattice fringes, while the homologous fast Fourier transformation (FFT) image further demonstrated the amorphous nature of CoOOH (the inset of Fig. 5(c)). Meanwhile, the great mass of samples still remains polycrystalline structure through a typical circle pattern (the inset FFT images in Fig. 5(c)).

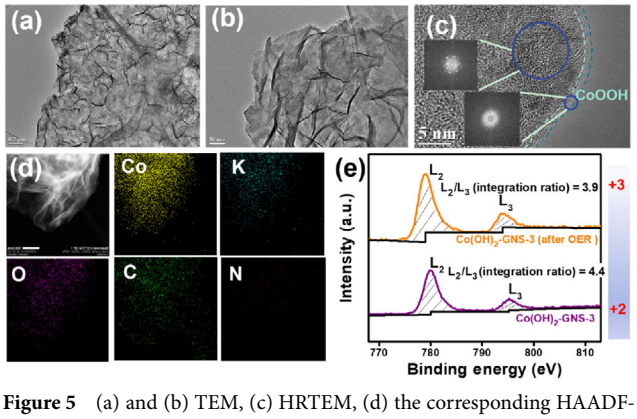


**Figure 5** (a) and (b) TEM, (c) HRTEM, (d) the corresponding HAADF-STEM images and EDS mapping images and (e) EELS spectra of $Co(OH)_2$-GNS-3 after OER process.

## 2.3 DFT analysis and electron holography

Density functional theory (DFT) calculation was employed to further investigate the prominent electrocatalytic activity and correlation between GO and α-$Co(OH)_2$ NS. The relative computation methods were described in the ESM. Generally, the OER processes in an alkaline solution [46] is as follows

$$* + OH^- \rightarrow HO^* + e^- \quad (1)$$

$$HO^* + OH^* \rightarrow O^* + e^- + H_2O \quad (2)$$

$$O^* + OH^- \rightarrow HOO^* + e^- \quad (3)$$

$$HOO^* + OH^- \rightarrow O_2^* + e^- + H_2O \quad (4)$$

$$O_2^* \rightarrow * + O_2 \quad (5)$$

where * stands for the catalyst. During the reaction process, HO*, O*, HOO*, and $O_2$* are formed, and ultimately the * and $O_2$ are gained. Previous reports have shown that the intrinsic activity was estimated by the largest standard Gibbs free energy difference of the rate-determining step for the OER [47, 48], which is the third step for α-$Co(OH)_2$ NS and the second step for $Co(OH)_2$-GNS. Figures 6(a)–6(d) present the optimized atomic structure model and Fig. S22 in the ESM indicates OH, O and OOH species adsorbed on α-$Co(OH)_2$ and $Co(OH)_2$-GNS catalyst. The free energy changes profiles for α-$Co(OH)_2$ NS and $Co(OH)_2$-GNS in every OER process are apparently downhill at an applied potential of 1.54 and 1.51 V, respectively (Fig. 6(e)). By calculation, the overpotential of sandwich-like $Co(OH)_2$-GNS is 0.28 V, lower than pristine α-$Co(OH)_2$ obviously. Accordingly, self-transforming $Co(OH)_2$-GNS exhibits a superior electrocatalytic performance, which can enable the intermediates and product lower energy levels than individual α-$Co(OH)_2$ to realize outstanding OER property.

Active sites consisting of high-density of charges/electrons determine the final OER performance which is urgently needed to be addressed. Furthermore, to comprehensively clarify the relationship between charge distribution of interfacial/in-plane area and OER performance of $Co(OH)_2$-GNS samples, an off-axis electron holography analysis was employed (Fig. 7), which can effectively to establish the correlation between the electrocatalytic properties and local electric field sandwiched between the $Co(OH)_2$/GNS sheet components. Diagrammatic drawing (Figs. 7(a), 7(e), and 7(i)) of the morphology structure for the $Co(OH)_2$-GNS demonstrated that the α-$Co(OH)_2$ NS were decorated onside GO surface, displaying the typical interfacial structure between α-$Co(OH)_2$ NS and GO (Figs. 7(a) and 7(i)) and in-plane stacked structure among α-$Co(OH)_2$ NS (Fig. 7(e)).

After reconstructing the electron holograms (Figs. 7(b), 7(f), and 7(j)), the phase shift images (Figs. 7(c), 7(g), and 7(k)) were

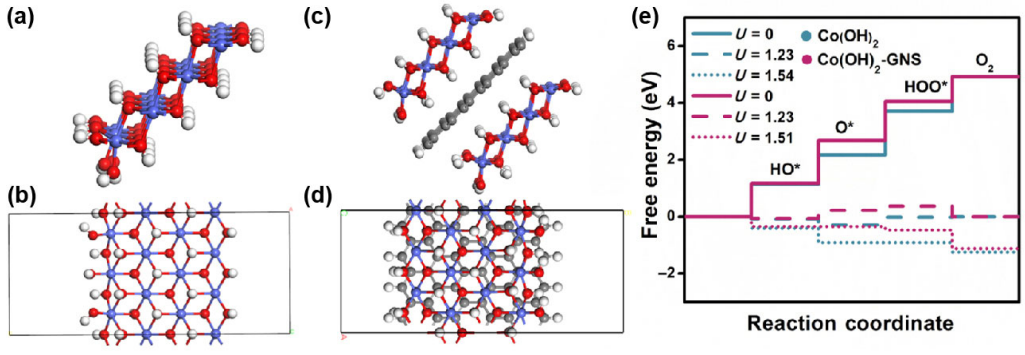


**Figure 6** DFT calculation. The optimized atomic structure model and theoretical calculation analysis of the catalysts: (a) and (c) top views and (b) and (d) side views of the model structure of $Co(OH)_2$ and $Co(OH)_2$-GNS (red: oxygen; blue: cobalt; grey: carbon; white: hydrogen); (e) the energy profiles for the OER pathway on the pristine $Co(OH)_2$ and $Co(OH)_2$-GNS catalyst.

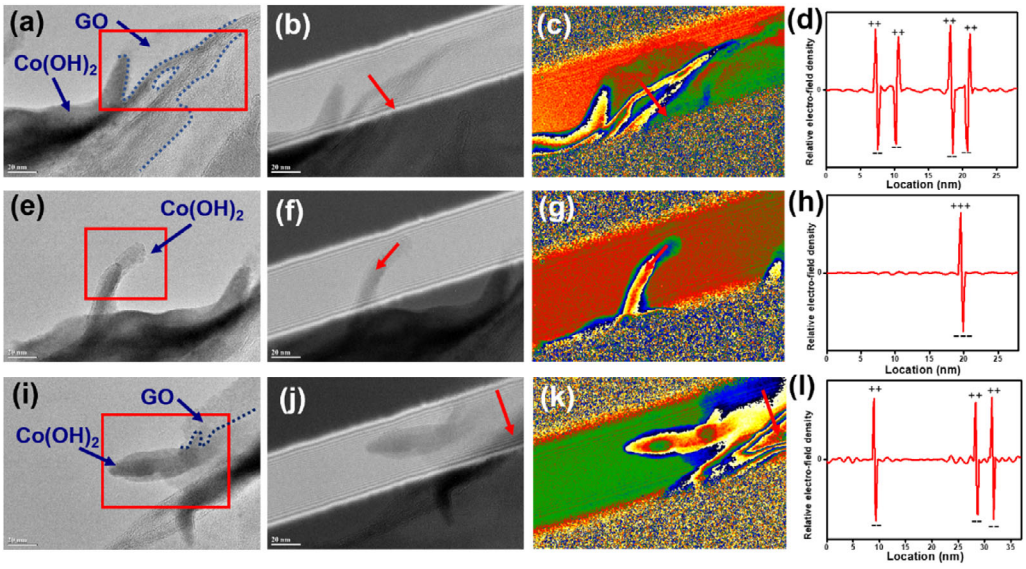


**Figure 7** Electron holography. The TEM images (a), (e), and (i), electron holography images (b), (f), and (j), reconstructed phase images (c), (g), and (k) and the coressponding charge density distribution line profiles (d), (h), and (l) in the region of the red arrow for the $Co(OH)_2$-GNS-3 composites.

acquired. Line profile of charge density distribution crossing from the GO substrate to MOF-derived NS revealed that the redistribution of interfacial charge occurs due to the existence of the interfacial barrier formed by GO and α-$Co(OH)_2$ NS (Figs. 7(c) and 7(k), red arrows). The well-defined heterointerface formed by ultrathin α-$Co(OH)_2$ NS and GO could considerably expose more catalytic sites and greatly enhance the electronic transfer. Moreover, our advantageous structure feature includes the in-plane interfaces stacked by abundant of ultrathin α-$Co(OH)_2$ NS, which shows remarkable charge polarization with significant variation from positive charges to negative electrons (Fig. 7(h), scanning from one NS to the neighbor one). In most cases, our structure design provides more complicated interface including both $Co(OH)_2$–GNS and ultrathin $Co(OH)_2$ NS–$Co(OH)_2$ NS within one structure unit at the same time, which contributes strong interfacial polarization and electrochemical active centers (Fig. 7(l)) [49]. The electron motion requested by OER can be effectively accelerated by the local polarized electric field formed by the multiply surface/interface of α-$Co(OH)_2$ NS and GO, thus reducing the free energy of the intermediates and products and improving the electrocatalytic performance.

## 3 Conclusion

In summary, via a facile one-step self-transformation synthesis, we have developed ultrathin ZIF-67-derived Co-based NS modified GO support with sandwich-like topography, which holds an effective and stable OER electrocatalyst. The optimized $Co(OH)_2$-GNS sample exhibits a low overpotential of 259 mV at a current density of 10 $mA{\cdot}cm^{-2}$, small Tafel slope of 85.9 $mV{\cdot}dec^{-1}$ and good durability. The outstanding OER property of the $Co(OH)_2$-GNS was reasonably demonstrated, employing off-axis electron holography and DFT calculations. The OER electron transfer can be accelerated by the interfacial and in-plane charge polarization and local electric field. The charged surfaces of $Co(OH)_2$-GNS are more efficient for expediting intermediates sorption and enhancing the homologous catalytic property. Our advantageous structure can provide ample active sites, good conductivity and strong interfacial charge polarization during electrolysis. This work will pave a novel way to design advanced self-transformation materials as substitution of noble metal-free electrocatalysts for clean energy utilization.

## 4 Experimental section

### 4.1 Materials

All chemicals were used as received without any further purification. KOH and methanol (AR, 99.5%) were purchased from Sigma-Aldrich. $Co(NO_3)_2{\cdot}6H_2O$ (99.99%) and 2-methylimidazole (%) were purchased from Sinopharm Group Chemical Reagent Co., Ltd. Deionized water obtained from Milli-Q system (Millipore, Bedford, MA, USA) was used in all experiments.

### 4.2 Synthesis of $Co(OH)_2$-GNS-*x*

Graphite oxide was synthesized through a improved Hummers approach [24]. After that, 8 mmol $Co(NO_3)_2{\cdot}6H_2O$ and 30 mg GO were dispersed in 40 mL methanol. 2-Methylimidazole (8 mmol) was dissolved in 40 mL methanol. After ultrasonication for 10 min, the 2-methylimidazole solution was poured into the metal salt and GO solution and the resulting solution was ultrasonication for 12 h (40 kHz). The solid product was collected by centrifugation after washing with pure methanol. Finnaly, the specimen was dried at 60 °C for 6 h and named $Co(OH)_2$-GNS-3. The preparation process of $Co(OH)_2$-GNS-*x* ($x$ = 1, 2, 4, 5) composite was same as that of $Co(OH)_2$-GNS-3, except that content change of $Co(NO_3)_2{\cdot}6H_2O$, 2-methylimidazole and methanol listed at Table S1 in the ESM.

### 4.3 Synthesis of ZIF-67, $Co(OH)_2$, Co-ZIF-1 and Co-ZIF-2

Firstly, a certain amount of $Co(NO_3)_2{\cdot}6H_2O$ (1.0 mmol for ZIF-67, 2.0 mmol for Co-ZIF-1, 3.0 mmol for Co-ZIF-2 and 4.0 mmol for $Co(OH)_2$) was dissolved in 20.0 mL of methanol. Then, 2-methylimidazole (4.0 mmol) was dispersed in 20.0 mL of methanol before adding into the former pink cobalt nitrate $Co(NO_3)_2{\cdot}6H_2O$ solution. The mixed solution was aging for 24 h. Purple or khaki solids were collected, washed with methanol and dried at 60 °C overnight.

### 4.4 Characterization

The as-synthesized samples ware characterized by XRD (Bruker, D8-Advance X-ray diffractometer using with Ni-filtered Cu Kα radiation, $\lambda$ = 0.154 nm). The morphology and size of the $Co(OH)_2$-GNS products were assessed using a field-emission

scanning electron microscope (FESEM, S-4800) and transmission electron microscope (JEOL, JEM-2100F, 200 kV). AFM was conducted on Bruker Dimension ICON SPM using peak force mode. Nitrogen adsorption isotherm measurements were carried out at 77 K with a Micromeritics Tristar 3020 analyzer. Raman spectra were recorded at room temperature in ambient conditions on a Renishow Invia spectrometer equipped with a Leica DMLM confocal microscope and a CCD detector with a 514 nm laser excitation. FT-IR spectra were obtained in transmission mode on a Nicolet 8700 FT-IR. The XPS measurements were recorded on KRATOS Axis Ultra Dld equipped with a monochromatic X-ray source (Al K$\alpha$, $h\nu$ = 1,486.6 eV). Before the spectra acquisition the samples were pelletized and outgassed for 1 h at 50 °C, and the pressure for the analysis chamber was $10^{-9}$ mbar.

## Acknowledgements

This work was supported by the National Basic Research Program of China (No. 2018YFA209102) and the National Natural Science Foundation of China (Nos. 11727807, 51725101, 51672050, and 61790581).

**Electronic Supplementary Material**: Supplementary material (additional experimental and DFT calculation details of the MOF-derived composites, figures showing details of the characterization and studies of $Co(OH)_2$-GNS-$x$, comparison of electrochemical performance) is available in the online version of this article at https://doi.org/10.1007/s12274-020-2701-4.

## References

[1] Chen, P. Z.; Zhou, T. P.; Xing, L. L.; Xu, K.; Tong, Y.; Xie, H.; Zhang, L. D.; Yan, W. S.; Chu, W. S.; Wu, C. Z. et al. Atomically dispersed iron-nitrogen species as electrocatalysts for bifunctional oxygen evolution and reduction reactions. *Angew. Chem., Int. Ed.* **2017**, *56*, 610–614.

[2] Gao, R.; Yan, D. P. Recent development of Ni/Fe-based micro/nanostructures toward photo/electrochemical water oxidation. *Adv. Energy Mater*., in press, DOI: 10.1002/aenm.20190095.

[3] Chen, J. D.; Zheng, F.; Zhang, S. J.; Fisher, A.; Zhou, Y.; Wang, Z. Y.; Li, Y. Y.; Xu, B. B.; Li, J. T.; Sun, S. G. Interfacial interaction between FeOOH and Ni–Fe LDH to modulate the local electronic structure for enhanced OER electrocatalysis. *ACS Catal.* **2018**, *8*, 11342–11351.

[4] Ma, Y.; Chu, J. Y.; Li, Z. N.; Rakov, D.; Han, X. J.; Du, Y. C.; Song, B.; Xu, P. Homogeneous metal nitrate hydroxide nanoarrays grown on nickel foam for efficient electrocatalytic oxygen evolution. *Small* **2018**, *14*, 1803783.

[5] Guo, Z. G.; Ye, W.; Fang, X. Y.; Wan, J.; Ye, Y. Y.; Dong, Y. Y.; Cao, D.; Yan, D. P. Amorphous cobalt-iron hydroxides as high-efficiency oxygen-evolution catalysts based on a facile electrospinning process. *Inorg. Chem. Front.* **2019**, *6*, 687–693.

[6] Li, Y. Z.; Abbott, J.; Sun, Y. C.; Sun, J. M.; Du, Y. C.; Han, X. J.; Wu, G.; Xu, P. Ru nanoassembly catalysts for hydrogen evolution and oxidation reactions in electrolytes at various pH values. *Appl. Catal. B: Environ.* **2019**, *258*, 117952.

[7] Banerjee, R.; Phan, A.; Wang, B.; Knobler, C.; Furukawa, H.; O'Keeffe, M.; Yaghi, O. M. High-throughput synthesis of zeolitic imidazolate frameworks and application to $CO_2$ capture. *Science* **2008**, *319*, 939–943.

[8] Cao, F. F.; Zhao, M. T.; Yu, Y. F.; Chen, B.; Huang, Y.; Yang, J.; Cao, X. H.; Lu, Q. P.; Zhang, X.; Zhang, Z. C. et al. Synthesis of two-dimensional $CoS_{1.097}$/nitrogen-doped carbon nanocomposites using metal-organic framework nanosheets as precursors for supercapacitor application. *J. Am. Chem. Soc.* **2016**, *138*, 6924–6927.

[9] Hu, H.; Zhang, J. T.; Guan, B. Y.; Lou, X. W. Unusual formation of CoSe@carbon nanoboxes, which have an inhomogeneous shell, for efficient lithium storage. *Angew. Chem., Int. Ed.* **2016**, *55*, 9514–9518.

[10] Peng, S.; Bie, B. L.; Sun, Y. Z. S.; Liu, M.; Cong, H. J.; Zhou, W. T.; Xia, Y. C.; Tang, H.; Deng, H. X.; Zhou, X. Metal-organic frameworks for precise inclusion of single-stranded DNA and transfection in immune cells. *Nat. Commun.* **2018**, *9*, 1293.

[11] Rungtaweevoranit, B.; Baek, J.; Araujo, J. R.; Archanjo, B. S.; Choi, K. M.; Yaghi, O. M.; Somorjai, G. A. Copper nanocrystals encapsulated in Zr-based metal-organic frameworks for highly selective $CO_2$ hydrogenation to methanol. *Nano Lett.* **2016**, *16*, 7645–7649.

[12] Zhao, S. L.; Wang, Y.; Dong, J. C.; He, C. T.; Yin, H. J.; An, P. F.; Zhao, K.; Zhang, X. F.; Gao, C.; Zhang, L. J. et al. Ultrathin metal–organic framework nanosheets for electrocatalytic oxygen evolution. *Nat. Energy* **2016**, *1*, 16184.

[13] Duan, J. J.; Chen, S.; Zhao, C. Ultrathin metal-organic framework array for efficient electrocatalytic water splitting. *Nat. Commun.* **2017**, *8*, 15341.

[14] Yang, J.; Zhang, F. Y.; Lu, H. Y.; Hong, X.; Jiang, H. L.; Wu, Y. E.; Li, Y. D. Hollow Zn/Co ZIF particles derived from core-shell ZIF-67@ZIF-8 as selective catalyst for the semi-hydrogenation of acetylene. *Angew. Chem., Int. Ed.* **2015**, *54*, 10889–10893.

[15] Li, Y. Z.; Niu S. Q.; Rakov, D.; Wang, Y.; Cabán-Acevedo, M.; Zheng, S. J.; Song, B.; Xu, P. Metal organic framework-derived CoPS/N-doped carbon for efficient electrocatalytic hydrogen evolution. *Nanoscale* **2018**, *10*, 7291–7297.

[16] Han, M. K.; Yin, X. W.; Li, X. L.; Anasori, B.; Zhang, L. T.; Cheng, L. F.; Gogotsi, Y. Laminated and two-dimensional carbon-supported microwave absorbers derived from MXenes. *ACS Appl. Mater. Interfaces* **2017**, *9*, 20038–20045.

[17] Li, Y.; Zhang, L.; Xiang, X.; Yan, D. P.; Li, F. Engineering of ZnCo-layered double hydroxide nanowalls toward high-efficiency electrochemical water oxidation. *J. Mater. Chem. A* **2014**, *2*, 13250–13258.

[18] Xu, C. Y.; Li, Q. H.; Shen, Q. L.; Yuan, Z.; Ning, J. Q.; Zhong, Y. J.; Zhang, Z. Y.; Hu, Y. A facile sequential ion exchange strategy to synthesize $CoSe_2$/$FeSe_2$ double-shelled hollow nanocuboids for the highly active and stable oxygen evolution reaction. *Nanoscale* **2019**, *11*, 10738–10745.

[19] Wu, J. J.; Zhang, D.; Wang, Y.; Wan, Y.; Hou, B. R. Catalytic activity of graphene–cobalt hydroxide composite for oxygen reduction reaction in alkaline media. *J. Power Sources* **2012**, *198*, 122–126.

[20] Wang, L.; Li, X.; Li, Q. Q.; Zhao, Y. H.; Che, R. C. Enhanced polarization from hollow cube-like $ZnSnO_3$ wrapped by multiwalled carbon nanotubes: As a lightweight and high-performance microwave absorber. *ACS Appl. Mater. Interfaces* **2018**, *10*, 22602–22610.

[21] Liu, H. D.; Chen, Z. L.; Zhou, L.; Li, X.; Pei, K.; Zhang, J.; Song, Y.; Fang, F.; Che, R. C.; Sun, D. L. Rooting bismuth oxide nanosheets into porous carbon nanoboxes as a sulfur immobilizer for lithium–sulfur batteries. *J. Mater. Chem. A* **2019**, *7*, 7074–7081.

[22] Yao, Y.; Li, C.; Huo, Z. L.; Liu, M.; Zhu, C. X.; Gu, C. Z.; Duan, X. F.; Wang, Y. G.; Gu, L.; Yu, R. C. *In situ* electron holography study of charge distribution in high-$\kappa$ charge-trapping memory. *Nat. Commun.* **2013**, *4*, 2764.

[23] Rau, W. D.; Schwander, P.; Baumann, F. H.; Höppner, W.; Ourmazd, A. Two-dimensional mapping of the electrostatic potential in transistors by electron holography. *Phys. Rev. Lett.* **1999**, *82*, 2614–2617.

[24] Lin, Z. Y.; Waller, G.; Liu, Y.; Liu, M. L.; Wong, C. P. Facile synthesis of nitrogen-doped graphene via pyrolysis of graphene oxide and urea, and its electrocatalytic activity toward the oxygen-reduction reaction. *Adv. Energy Mater.* **2012**, *2*, 884–888.

[25] Firmiano, E. G. S.; Cordeiro, M. A. L.; Rabelo, A. C.; Dalmaschio, C. J.; Pinheiro, A. N.; Pereira, E. C.; Leite, E. R. Graphene oxide as a highly selective substrate to synthesize a layered $MoS_2$ hybrid electrocatalyst. *Chem. Commun.* **2012**, *48*, 7687–7689.

[26] Hu, W. H.; Shang, X.; Han, G. Q.; Dong, B.; Liu, Y. R.; Li, X.; Chai, Y. M.; Liu, Y. Q.; Liu, C. G. $MoS_x$ supported graphene oxides with different degree of oxidation as efficient electrocatalysts for hydrogen evolution. *Carbon* **2016**, *100*, 236–242.

[27] Sun, J. Q.; Yang, D. J.; Lowe, S.; Zhang, L. J.; Wang, Y. Z.; Zhao, S. L.; Liu, P. R.; Wang, Y.; Tang, Z. Y.; Zhao, H. J. et al. Sandwich-like reduced graphene oxide/carbon black/amorphous cobalt borate nanocomposites as bifunctional cathode electrocatalyst in rechargeable zinc-air batteries. *Adv. Energy Mater.* **2018**, *8*, 1801495.

[28] Yan, C. S.; Fang, Z. W.; Lv, C. D.; Zhou, X.; Chen, G.; Yu, G. H. Significantly improving lithium-ion transport via conjugated anion intercalation in inorganic layered hosts. *ACS Nano* **2018**, *12*, 8670–8677.

[29] Liu, X.; Wang, L.; Yu, P.; Tian, C. G.; Sun, F. F.; Ma, J. Y.; Li, W.; Fu, H. G. A stable bifunctional catalyst for rechargeable zinc-air batteries: Iron-cobalt nanoparticles embedded in a nitrogen-doped 3D carbon matrix. *Angew. Chem., Int. Ed.* **2018**, *57*, 16166–16170.

[30] Yan, J.; Fan, Z. J.; Sun, W.; Ning, G. Q.; Wei, T.; Zhang, Q.; Zhang, R. F.; Zhi, L. J.; Wei, F. Advanced asymmetric supercapacitors based on $Ni(OH)_2$/graphene and porous graphene electrodes with high energy density. *Adv. Funct. Mater.* **2012**, *22*, 2632–2641.

[31] Yang, J.; Yu, C.; Hu, C.; Wang, M.; Li, S. F.; Huang, H. W.; Bustillo, K.; Han, X. T.; Zhao, C. T.; Guo, W. et al. Surface-confined fabrication of ultrathin nickel cobalt-layered double hydroxide nanosheets for high-performance supercapacitors. *Adv. Funct. Mater.* **2018**, *28*, 1803272.

[32] Pei, T.; Zhang, Z. Q.; Li, B. H.; Vinu, M.; Lin, C. H.; Lee, S. Raman observation of the "volcano curve" in the formation of carbonized metal–organic frameworks. *J. Phys. Chem. C* **2017**, *121*, 22939–22947.

[33] Ye, F.; Song, Q.; Zhang, Z. C.; Li, W.; Zhang, S. Y.; Yin, X. W.; Zhou, Y. Z.; Tao, H. W.; Liu, Y. S.; Cheng, L. F. et al. Direct growth of edge-rich graphene with tunable dielectric properties in porous $Si_3N_4$ ceramic for broadband high-performance microwave absorption. *Adv. Funct. Mater.* **2018**, *28*, 1707205.

[34] Liu, X. L.; Wu, J. J.; Huang, X. L.; Liu, Z. W.; Zhang, Y.; Wang, M.; Che, R. C. Predominant growth orientation of $Li_{1.2}(Mn_{0.4}Co_{0.4})O_2$ cathode materials produced by the NaOH compound molten salt method and their enhanced electrochemical performance. *J. Mater. Chem. A* **2014**, *2*, 15200–15208.

[35] Li, S. S.; Zhao, Y. H.; Liu, Z. W.; Yang, L. T.; Zhang, J.; Wang, M.; Che, R. C. Flexible graphene-wrapped carbon nanotube/graphene@$MnO_2$ 3D multilevel porous film for high-performance lithium-ion batteries. *Small* **2018**, *14*, 1801007.

[36] Shang, L.; Yu, H. J.; Huang, X.; Bian, T.; Shi, R.; Zhao, Y. F.; Waterhouse, G. I. N.; Wu, L. Z.; Tung, C. H.; Zhang, T. R. Well-dispersed ZIF-derived Co,N-Co-doped carbon nanoframes through mesoporous-silica-protected calcination as efficient oxygen reduction electrocatalysts. *Adv. Mater.* **2016**, *28*, 1668–1674.

[37] Arif, M.; Yasin, G.; Shakeel, M.; Mushtaq, M. A.; Ye, W.; Fang, X. Y.; Ji, S. F.; Yan, D. P. Hierarchical CoFe-layered double hydroxide and g-$C_3N_4$ heterostructures with enhanced bifunctional photo/electrocatalytic activity towards overall water splitting. *Mater. Chem. Front.* **2019**, *3*, 520–531.

[38] Kang, B. K.; Im, S. Y.; Lee, J.; Kwag, S. H.; Kwon, S. B.; Tiruneh, S.; Kim, M. J.; Kim, J. H.; Yang, W. S.; Lim, B. et al. *In-situ* formation of MOF derived mesoporous $Co_3N$/amorphous N-doped carbon nanocubes as an efficient electrocatalytic oxygen evolution reaction. *Nano Res.* **2019**, *12*, 1605–1611.

[39] Jiang, Y.; Deng, Y. P.; Fu, J.; Lee, D. U.; Liang, R. L.; Cano, Z. P.; Liu, Y. S.; Bai, Z. Y.; Hwang, S.; Yang, L. et al. Interpenetrating triphase cobalt-based nanocomposites as efficient bifunctional oxygen electrocatalysts for long-lasting rechargeable Zn-air batteries. *Adv. Energy Mater.* **2018**, *8*, 1702900.

[40] Qiao, M. T.; Lei, X. F.; Ma, Y.; Tian, L. D.; He, X. W.; Su, K. H.; Zhang, Q. Y. Application of yolk-shell $Fe_3O_4$@N-doped carbon nanochains as highly effective microwave-absorption material. *Nano Res.* **2018**, *11*, 1500–1519.

[41] Gao, R.; Yan, D. P. Fast formation of single-unit-cell-thick and defect-rich layered double hydroxide nanosheets with highly enhanced oxygen evolution reaction for water splitting. *Nano Res.* **2018**, *11*, 1883–1894.

[42] Bao, J.; Wang, Z. L.; Xie, J. F.; Xu, L.; Lei, F. C.; Guan, M. L.; Huang, Y. P.; Zhao, Y.; Xia, J. X.; Li, H. M. The CoMo-LDH ultrathin nanosheet as a highly active and bifunctional electrocatalyst for overall water splitting. *Inorg. Chem. Front.* **2018**, *5*, 2964–2970.

[43] Zou, H. Y.; He, B. W.; Kuang, P. Y.; Yu, J. G.; Fan, K. Metal-organic framework-derived nickel-cobalt sulfide on ultrathin mxene nanosheets for electrocatalytic oxygen evolution. *ACS Appl. Mater. Interfaces* **2018**, *10*, 22311–22319.

[44] Shi, P. C.; Yi, J. D.; Liu, T. T.; Li, L.; Zhang, L. J.; Sun, C. F.; Wang, Y. B.; Huang, Y. B.; Cao, R. Hierarchically porous nitrogen-doped carbon nanotubes derived from core–shell ZnO@zeolitic imidazolate framework nanorods for highly efficient oxygen reduction reactions. *J. Mater. Chem. A* **2017**, *5*, 12322–12329.

[45] Pan, Y.; Sun, K. A.; Liu, S. J.; Cao, X.; Wu, K. L.; Cheong, W. C.; Chen, Z.; Wang, Y.; Li, Y.; Liu, Y. Q. et al. Core-shell ZIF-8@ZIF-67-derived CoP nanoparticle-embedded N-doped carbon nanotube hollow polyhedron for efficient overall water splitting. *J. Am. Chem. Soc.* **2018**, *140*, 2610–2618.

[46] Feng, J. X.; Xu, H.; Dong, Y. T.; Ye, S. H.; Tong, Y. X.; Li, G. R. FeOOH/Co/FeOOH hybrid nanotube arrays as high-performance electrocatalysts for the oxygen evolution reaction. *Angew. Chem., Int. Ed.* **2016**, *55*, 3694–3698.

[47] Man, I. C.; Su, H. Y.; Calle-Vallejo, F.; Hansen, H. A.; Martínez, J. I.; Inoglu, N. G.; Kitchin, J.; Jaramillo, T. F.; Nørskov, J. K.; Rossmeisl, J. Universality in oxygen evolution electrocatalysis on oxide surfaces. *ChemCatChem* **2011**, *3*, 1159–1165.

[48] Jin, H. Y.; Mao, S. J.; Zhan, G. P.; Xu, F.; Bao, X. B.; Wang, Y. Fe incorporated α-$Co(OH)_2$ nanosheets with remarkably improved activity towards the oxygen evolution reaction. *J. Mater. Chem. A* **2017**, *5*, 1078–1084.

[49] Jiao, W. L.; Chen, C.; You, W. B.; Zhang, J.; Liu, J. W.; Che, R. C. Yolk-shell Fe/$Fe_4N$@Pd/C magnetic nanocomposite as an efficient recyclable ORR electrocatalyst and SERS substrate. *Small* **2019**, *15*, 1805032.